



Available online at www.sciencedirect.com



International Journal of Plasticity 24 (2008) 2278–2297

INTERNATIONAL JOURNAL OF
Plasticity

www.elsevier.com/locate/ijplas

Investigation of three-dimensional aspects of grain-scale plastic surface deformation of an aluminum oligocrystal

Z. Zhao ^a, M. Ramesh ^b, D. Raabe ^b, A.M. Cuitiño ^c, R. Radovitzky ^{a,*}

^a *Department of Aeronautics and Astronautics, Massachusetts Institute of Technology, Cambridge, MA, USA*

^b *Department for Microstructure Physics, Max-Planck-Institut für Eisenforschung, Düsseldorf, Germany*

^c *Department of Mechanical and Aerospace Engineering, Rutgers University, Piscataway, NJ, USA*

Received 31 August 2007; received in final revised form 17 January 2008

Available online 2 February 2008

Abstract

This is a study of plastic strain localization, surface roughening and of the origin of these phenomena in polycrystals. An oligocrystal aluminum sample with a single quasi-2D layer of coarse grains is plastically deformed under uniaxial tensile loading. During deformation, the history of strain localization, surface roughening, microstructure and in-grain fragmentation is carefully recorded. Using a crystal plasticity finite element model, corresponding high-resolution simulations are conducted. A series of comparisons identifying aspects of good and of less good match between model predictions and experiments is presented. The study suggests that the grain topology and microtexture have a significant influence on the origin of strain heterogeneity. Moreover, it suggests that the final surface roughening profiles are related both to the macro strain localization and to the intra-grain interaction. Finally slip lines observed on the surface of the samples are used to probe the activation of slip systems in detail. The study concludes with an assessment of the limitations of the crystal plasticity model.

© 2008 Elsevier Ltd. All rights reserved.

Keywords: Crystal plasticity; Grain interaction; Strain heterogeneity; EBSD; Strain mapping

* Corresponding author.

E-mail address: rapa@mit.edu (R. Radovitzky).

1. Introduction

Deformation heterogeneities, such as earing, surface roughening and necking, commonly occur during metal forming. Where their occurrence is not due to the prevailing macroscopic boundary conditions, generally it is related to the microstructure of the metal. It is with the latter that this study is concerned, and particularly with the relationship between the local crystallographic texture and the anisotropic mechanical interaction among individual grains. For instance, differently oriented grains can create substantial deformation incompatibilities between neighboring crystals owing to their mechanical anisotropy. Such incompatibilities can influence not only grain-to-grain interaction phenomena in the bulk, but also the formation of grain-scale roughening effects at the free sample surface.

These observations have been supported by an increasing number of experimental and computational studies of surface roughening phenomena (Becker, 1998; Beaudoin et al., 1998; Raabe et al., 2003; Shin et al., 2003; Zhao et al., 2004). For example, Becker's study (Becker, 1998) suggests that surface strain localization, strain hardening, crystallographic texture and material homogeneity all play important roles in surface roughening. Beaudoin et al. (1998) presented the first three-dimensional simulations of surface roughening, with results showing that grains of similar orientations can act collectively to define the overall roughening profile. Shin et al. (2003) showed in a recent study on b.c.c steel, that varying combinations of texture components can lead to different ridging shapes in b.c.c materials. Raabe et al. (2003) revealed that the aggregation status of certain texture components can lead to different ridging profiles in aluminum sheet. These studies have shown that the combination of experiments and simulations provides a synergistic approach for the analysis of grain-scale plasticity phenomena. However, a direct one-to-one comparison of grain-scale surface roughening profiles between experiments and simulation has yet to be presented.

In recent years, experiments on oligocrystals, i.e. samples containing only a small set of crystals with millimeter grain size, have focused attention on the deformation-induced plastic heterogeneity of polycrystals (Delaire et al., 2000; Raabe et al., 2001; Zhang and Tong, 2004; Cheonga and Busso, 2006). Oligocrystal samples have the advantage of allowing grain-scale heterogeneity phenomena to be magnified from the micro-level to a level clearly visible to the naked eye. More importantly – and especially when used in the crystal plasticity finite element models – they provide a bridge directly linking experimental observations with numerical studies.

A close look at the cited papers discloses some similarities between the experimental procedures and the simulation approaches used thus far. Firstly, all the oligocrystal samples had been cut to a single layer with a columnar grain shape through the thickness direction. This had the effect of eliminating the complexity of the interaction from grains beneath the visible surface layer. Secondly, grain orientation mapping using backscatter electron scattering diffraction (EBSD) techniques was applied to reveal the microtexture at the deformed and the undeformed state. Thirdly, surface strain localization in most of these studies was measured using digital image correlation (DIC) methods, which work by tracing pattern changes on the strained sample surface. Finally, the simulation tool predominantly used in these works was the finite element crystal plasticity (FEMCP) method, which provides a computational framework capable of addressing the complexity of the problem, including the mechanical grain interaction, the sample geometry, the loading

boundary condition, the grain topology, the grain orientation changes (or texture evolution), the microstructure information and the hardening response of the crystal (Kalidindi et al., 1992; Beaudoin et al., 1996; Sarma and Dawson, 1996; Buchheit et al., 1997; Mika and Dawson, 1999; Bate, 1999).

Delaire's simulation (Delaire et al., 2000) used the finite element crystal plasticity method to describe strain localization in an oligocrystal sample under uniaxial tension and to numerically trace the history of slip system activation. Using the more advanced DIC technique, Raabe et al. (2001) provided a detailed surface strain mapping of oligocrystal samples under plane strain compression and a simulation proving that this heterogeneity arises from the combination of the macroscopic boundary condition and the grain interaction. Probing more deeply the mechanism of slip systems activation, Zhang and Tong (2004) investigated the differences in the behavior of multicrystals tested under uniaxial conditions, versus the behavior predicted in Sachs and Taylor models. More recently, Cheonga and Busso (2006) proved using a similar strategy that the strain hardening behavior in polycrystals under uniaxial tension is further influenced by the in-grain misorientation distribution.

The framework adopted in these studies provided the motivation for comparing surface roughening behavior observed in experiments versus that suggested by simulations. Such comparison could provide insight into grain-scale roughening mechanisms, and could be used to validate the robustness of numerical models in the prediction of local surface displacements. With this motivation, a series of uniaxial tension tests were conducted and detailed diagnostics were obtained using EBSD, DIC and surface roughening measurements on an oligocrystal sample. In addition, numerical simulations of these tests were conducted using the finite element crystal plasticity method. The goal was to obtain a one-to-one comparison of the simulations with the experimental results, with particular emphasis on the evolution of surface roughening; and ultimately to obtain a detailed assessment of the accuracy and limitations of the modeling approach in capturing features of the experimental observations at the grain level.

This paper is organized as follows. Section 2 describes the sample preparation and the experimental procedures. Section 3 briefly reviews the crystal plasticity finite element model used. Section 4 presents the results and comparisons of the experimental observations and the numerical simulations. A discussion of the results is presented in Section 5. Finally, Section 6 closes the paper with a short summary and conclusions.

2. Sample preparation and experimental procedure

A coarse-grained tensile “dogbone” test sample was cut from a pure aluminum ingot which had been annealed at 600 °C for 48 h. The sample contained a quasi-2D layer of grains (average size about 3.5 mm) with columnar morphology along its thickness. The dimensions of the dogbone gauge section were confined to 21 mm (long), 8 mm (wide) and 1 mm (thick), owing to the size of the electron microscope chamber.

Grain boundary profiles and crystallographic orientation maps on the sample surface were determined using the electron backscatter diffraction (EBSD) technique. EBSD involves the measurement of local crystallographic orientations on a regular grid through the automated acquisition and analysis of Kikuchi patterns at a 100 μm step size, which provides sufficient spatial resolution to capture the variations on the deformation field at the mesoscale level. This resolution is consistent with the theory where dislocation struc-

tures are not explicitly considered. This measurement was conducted before tensile testing in order to obtain an initial orientation mapping, and repeated afterwards to obtain the texture distribution in the deformed state.

Uniaxial tensile deformation was performed on the dogbone using a special-purpose miniaturized tension test equipment. This equipment utilized two computerized moveable crossheads which held the center of the sample at a fixed position during the elongation. The experiments were conducted at a strain rate of $4.76 \times 10^{-5} \text{ s}^{-1}$ and ambient temperature to a final elongation of 15%.

To aid measurement of the evolution of surface strain localization, speckles were introduced on both surfaces of the sample prior to the tension test by a fine mist of paint. The variations in those patterns caused by the strain localization were recorded in a series of digital images taken on both sides of the sample at 10 s intervals. Finally, a detailed evolution history of the surface displacement field was calculated based on the geometrical changes of the surface patterns.

After the surface had been cleaned, the 3D surface topography of the specimens was measured using a white-light confocal microscope. In order to obtain the complete surface roughness profile of the dogbone sample, a series of small square areas of approximately $750 \mu\text{m}$ square were measured independently and then combined. Subsequently, detailed surface slip steps were measured using the same equipment at a much higher density, for the purpose of analyzing the activation of slip systems.

3. Finite element crystal plasticity model

The f.c.c. crystal plasticity constitutive model adopted in the calculations presented here corresponds to the explicit formulation presented in Kuchnicki et al. (2006). This particular formulation provides significant performance improvements over the original implicit formulation of the forest dislocation hardening model presented in Cuitiño and Ortiz (1992), thus rendering the model suitable for large-scale computations. For completeness, a summary of the formulation of the model is presented in this section.

The total deformation of a crystal is the result of two main mechanisms: dislocation motion within the active slip systems, and lattice distortion. Following Lee (1969), this points to a multiplicative decomposition

$$\mathbf{F} = \mathbf{F}^e \mathbf{F}^p \quad (1)$$

of the deformation gradient \mathbf{F} , into a plastic part \mathbf{F}^p , which accounts for the cumulative effect of dislocation motion, and an elastic part \mathbf{F}^e , which accounts for the remaining non-plastic deformation. Following Teodosiu (1969) and others (Asaro and Rice, 1977; Havner, 1973; Hill and Rice, 1972; Mandel, 1972; Rice, 1971), the authors assume that \mathbf{F}^p leaves the crystal lattice not only essentially undistorted, but also unrotated. Thus, the distortion and rotation of the lattice is contained in \mathbf{F}^e . This choice of kinematics uniquely determines the decomposition (1). By virtue of (1), the deformation power per unit of undeformed volume takes the form

$$\mathbf{P} : \dot{\mathbf{F}} = \bar{\mathbf{P}} : \dot{\mathbf{F}}^e + \bar{\Sigma} : \bar{\mathbf{L}}^p \quad (2)$$

where

$$\bar{\mathbf{P}} = \mathbf{P} \mathbf{F}^{pT} \bar{\Sigma} = \mathbf{F}^{eT} \mathbf{P} \mathbf{F}^{pT} \bar{\mathbf{L}}^p = \dot{\mathbf{F}}^p \mathbf{F}^{p-1} \quad (3)$$

Here, $\bar{\mathbf{P}}$ defines a first Piola–Kirchhoff stress tensor relative to the intermediate configuration $\bar{\mathcal{B}}_t$, and $\bar{\boldsymbol{\Sigma}}$ a stress measure conjugate to the plastic velocity gradients $\bar{\mathbf{L}}^p$ on $\bar{\mathcal{B}}_t$. The work-conjugacy relations expressed in (2) suggest plastic flow rules and elastic stress–strain relations of the general form

$$\bar{\mathbf{L}}^p = \bar{\mathbf{L}}^p(\bar{\boldsymbol{\Sigma}}, \bar{\mathbf{Q}}) \bar{\mathbf{P}} = \bar{\mathbf{P}}(\mathbf{F}^e, \bar{\mathbf{Q}}) \quad (4)$$

Here, $\bar{\mathbf{Q}}$ denotes some suitable set of internal variables defined on the intermediate configuration, for which equations of evolution, or hardening laws, are to be supplied. A standard exercise shows that the most general form of (2) consistent with the principle of material frame indifference is

$$\bar{\mathbf{P}} = \mathbf{F}^e \bar{\mathbf{S}}(\bar{\mathbf{C}}^e), \quad \bar{\mathbf{C}}^e = \mathbf{F}^{eT} \mathbf{F}^e \quad (5)$$

where $\bar{\mathbf{S}} = \bar{\mathbf{C}}^{e-1} \bar{\boldsymbol{\Sigma}}$ is a symmetric second Piola–Kirchhoff stress tensor relative to the intermediate configuration $\bar{\mathcal{B}}_t$, and $\bar{\mathbf{C}}^e$ is the elastic right Cauchy–Green deformation tensor on $\bar{\mathcal{B}}_t$. For most applications involving metals, elastic deformations are expected to be small compared to plastic deformations and a linear – but anisotropic – relation between $\bar{\mathbf{S}}$ and the elastic Lagrangian strain $\bar{\mathbf{E}}^e = (\bar{\mathbf{C}}^e - \mathbf{I})/2$ is generally assumed (Cuitiño and Ortiz, 1992). Higher-order moduli are given by Teodosiu (1982). From the kinematics of dislocation motion, it has been shown by Rice (1971) that (4) is of the form

$$\bar{\mathbf{L}}^p = \sum_{\alpha} \dot{\gamma}^{\alpha} \bar{\mathbf{s}}^{\alpha} \otimes \bar{\mathbf{m}}^{\alpha} \quad (6)$$

where $\dot{\gamma}^{\alpha}$ is the shear rate on slip system α and $\bar{\mathbf{s}}^{\alpha}$ and $\bar{\mathbf{m}}^{\alpha}$ are the corresponding slip direction and slip plane normal. At this point the assumption is commonly made that $\dot{\gamma}^{\alpha}$ depends on stress only through the corresponding resolved shear stress τ^{α} , i.e.,

$$\dot{\gamma}^{\alpha} = \dot{\gamma}^{\alpha}(\tau^{\alpha}, \bar{\mathbf{Q}}), \quad (7)$$

which is an extension of Schmid’s rule. If (7) is assumed to hold, then it was shown by Rice (1971) and by Mandel (1972) that the flow rule (6) derives from a viscoplastic potential.

In order to complete the constitutive description of the crystal, relations governing the evolution of plastic slip and internal variables $\bar{\mathbf{Q}}$ must be provided. In this work, the authors adopt the forest dislocation hardening model for f.c.c. metals of Cuitiño and Ortiz (1992). For completeness, a synopsis of the main assumptions of the model, and of the key constitutive relations is provided below. For a detailed history of pioneering studies of finite crystal deformation and review of classic experimental work on crystal hardening Havner’s book may be consulted (Havner, 1992).

The rate of shear deformation on slip system α is given by a power-law of the form:

$$\dot{\gamma}^{\alpha} = \begin{cases} \dot{\gamma}_0 \left[\left(\frac{\tau^{\alpha}}{g^{\alpha}} \right)^{1/m} - 1 \right] & \text{if } \tau^{\alpha} \geq 0 \\ 0 & \text{otherwise} \end{cases} \quad (8)$$

In this expression, m is the strain-rate sensitivity exponent, $\dot{\gamma}_0$ is a reference shear strain rate and g^{α} is the current shear flow stress on slip system α . Implicit in the form in which (8) is written is the convention of differentiating between the positive and negative slip directions $\pm \bar{\mathbf{m}}^{\alpha}$ for each slip system, whereas the slip rates $\dot{\gamma}^{\alpha}$ are constrained to be nonnegative. This rate-dependency law is slightly different from (Cuitiño and Ortiz, 1992) in that

its multiple root has been shifted. As has been noted by several authors (McGinty, 2001; Ling et al., 2005; Kuchnicki et al., 2006), this mitigates the tendency of the original model to predict unrealistic values of slip for $\frac{\tau_c^\alpha}{g^\alpha}$ much different from unity.

An analysis utilizing a crystal hardening theory based on statistical mechanics shows that for multiple slip, the evolution of the flow stresses is found to be governed by a *diagonal* hardening law:

$$\dot{g}^\alpha = \sum_{\alpha} h^{\alpha\alpha} \dot{\gamma}^\alpha \quad (9)$$

where $h^{\alpha\alpha}$ are the *diagonal* hardening moduli:

$$h^{\alpha\alpha} = \left(\frac{\tau_c^\alpha}{\gamma_c^\alpha}\right) \left(\frac{g^\alpha}{\tau_c^\alpha}\right)^3 \left\{ \cosh \left[\left(\frac{\tau_c^\alpha}{g^\alpha}\right)^2 \right] - 1 \right\} \text{no sum in } \alpha \quad (10)$$

In this expression,

$$\tau_c^\alpha = r\mu b\sqrt{\pi n^\alpha} \quad \text{and} \quad \gamma_c^\alpha = \frac{b\rho^\alpha}{2\sqrt{n^\alpha}} \text{no sum in } \alpha \quad (11)$$

are, respectively, a characteristic shear stress and strain for the slip system α . The values of τ_c^α and γ_c^α associated with the yielding observable during experiments, determine the location of the ‘bend’ in the resolved shear stress–slip strain curve. Thus, τ_c correlates well with the value of the flow stress determined by back extrapolation. In expressions (11), μ is the shear modulus which is evaluated as C_{44} , n^α is the density of obstacles in slip system α , ρ^α is the dislocation density in slip system α , b is the magnitude of the Burgers vector and r is a numerical coefficient (of the order of 0.3) that modulates the strength of the obstacle in slip plane α given by a pair of forest dislocations separated a distance l . This strength is estimated as

$$s^\alpha = r \frac{\mu b}{l}. \quad (12)$$

In order to complete the constitutive formulation, evolution equations for the obstacle density n^α and dislocation density ρ^α are provided. Evidently, n^α is a function of the dislocation densities in all the remaining systems. The experimental work of Franciosi and colleagues (Franciosi and Zaoui, 1982a,b, 1983; Franciosi, 1985a,b, 1988) suggests a dependence of the form

$$n^\alpha = \sum_{\beta} a^{\alpha\beta} \rho^\beta \quad (13)$$

Franciosi and Zaoui (1982a,b) have ranked and confirmed experimentally the relative values of the interaction matrix $a^{\alpha\beta}$ for the 12 slip systems belonging to the family of $\{111\}$ planes and $[110]$ directions in f.c.c. crystals. They classify the interactions according to whether the dislocations: (a) belong to the same system (interaction coefficient a_0); (b) fail to form junctions (interaction coefficient a_1); (c) form Hirth locks (interaction coefficient a_1); (d) form co-planar junctions (interaction coefficient a_1); (e) form glissile junctions (interaction coefficient a_2); or (f) form sessile Lomer–Cottrell locks (interaction coefficient a_3), with $a_0 \leq a_1 \leq a_2 \leq a_3$. Franciosi (1985b) has also found the interaction coefficients to be linearly dependent on the stacking fault energy of the crystal, with the degree of anisotropy increasing as the stacking fault energy decreases. More recently,

Table 1
Constitutive model parameters for pure aluminum (Cuitiño, 1996)

Parameter	Value	Parameter	Value
C_{11}	108 GPa	C_{12}	61 GPa
C_{44}	28.5 GPa	g_0	2 MPa
S	$135 \times 10^{-3} \text{ J/m}^2$	m	0.1
$\dot{\gamma}_0$	10 s^{-1}	γ_{sat}	0.5%
ρ_0	10^{12} m^{-2}	ρ_{sat}	10^{15} m^{-2}
b	$2.56 \times 10^{-10} \text{ m}$	μ	26 GPa

Havner (2005) has provided a general approach for determining probable active slip systems and their slip rates in diverse multislip conditions. Franciosi and Zaoui (1982a,b) results, however, are not in full agreement with those presented by Havner (2005).

Finally, an analytical expression for the evolution of ρ^z with the applied slip strain can be postulated by considering that the *dislocation production* is dominated by multiplication by cross glide, while the *dislocation annihilation* is proportional to the probability of having two dislocation segments of different sign in close proximity to each other. The resulting expression is given by

$$\rho^z = \rho_{\text{sat}} \left[1 - \left(1 - \frac{\rho_0}{\rho_{\text{sat}}} \right) e^{-\gamma^z / \gamma_{\text{sat}}} \right] \quad (14)$$

where ρ_{sat} and γ_{sat} are the saturation dislocation density and saturation shear slip – both determined by the multiplication and annihilation rates.

The values of the model parameters used in all the simulations presented in Section 4 are collected in Table 1. In specific boundary value problems, the assignment in space of the crystal's orientation completes the description of the constitutive response at the single crystal level.

4. Experimental results and corresponding simulation

4.1. Initial orientation mapping and mesh setup

The grain profiles on both the top surface (surface-A) and the bottom surface (surface-B) of the dogbone sample's gauge section obtained by EBSD are shown in Fig. 1. The similarity of the grain profiles on each side suggests that the grain boundaries remain ostensibly perpendicular to the surface of the sample throughout. However, there are exceptions to this and for some crystals the difference between the two surfaces is also evident. For example, grain-2 and grain-5 on the left side of surface-A disappear on the opposite surface-B (Fig. 1a and b). At the same time, two more grains, grain-21 and grain-22, show up along the bottom edge of surface-B. The difference between the grain numbers on each surface and on the grain shape, indicates that, in some cases, that shape is not perfectly columnar through the thickness.

In Fig. 1a and b, the orientation difference is marked using different colors.¹ In addition, the overall orientation distribution is plotted in {001} pole figures (Fig. 1c and d).

¹ For interpretation of the references to color in Figs. 1 and 5, the reader is referred to the web version of this article.

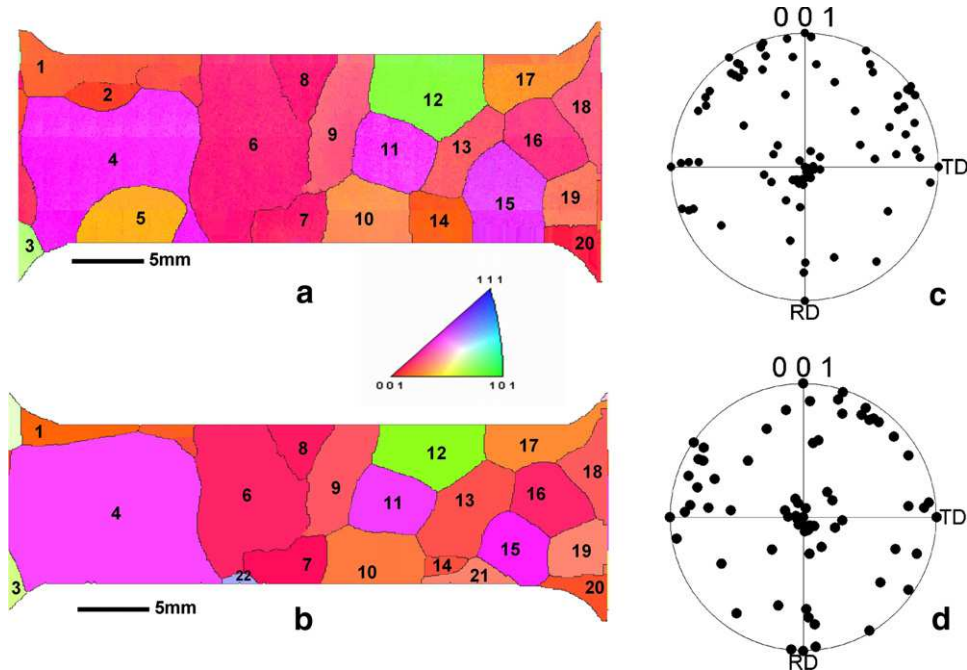


Fig. 1. Surface grain profiles and orientation distribution obtained by EBSD. (a) Grain shape on top surface identified as surface-A. (b) Grain shape on bottom surface identified as surface-B obtained by mirroring the pixels in the image file in order to facilitate the identification of individual grains. (c) Overall orientation distribution on surface-A plotted in $\{001\}$ pole figure. (d) Overall orientation distribution on surface-B plotted in $\{001\}$ pole figure. The color indicates the orientation difference in (a) and (b). A 5° misorientation is used as a threshold to identify the grain boundaries.

It is found that in this sample most of the grains occupy a texture component in the vicinity of the *twisted* Cube orientation. That is, most of the grains align their $[001]$ directions parallel to the surface normal, and at the same time they are slightly rotated about this $[001]$ axis. To aid visualization of the orientation difference between each grain, a 5° misorientation measure is used to illustrate the grain boundary profiles, as shown in Fig. 1a and b.

The mesh of the finite element model was created by mapping the geometry of the grain boundaries according to the EBSD measurement (Fig. 2). The spatial resolution of the mesh is consistent with the theory, where the dislocation structures are not explicitly accounted for. Because the real sample did not have a perfectly columnar shape, this mesh was based on the grain distribution on surface-A only, by extruding the grain boundary skeleton lines from surface-A in the normal through-thickness direction up to surface-B. As a result, all of the grains in the model have a perfectly columnar shape and a flat boundary. This approach avoids the complexity involved in representing the grain shape in 3D. The implications of this assumption are discussed in Section 5. After the mesh is created, each grain is assigned a specific orientation obtained from the EBSD measurement. Therefore, each individual grain is assumed to have a uniform orientation distribution in the undeformed configuration.

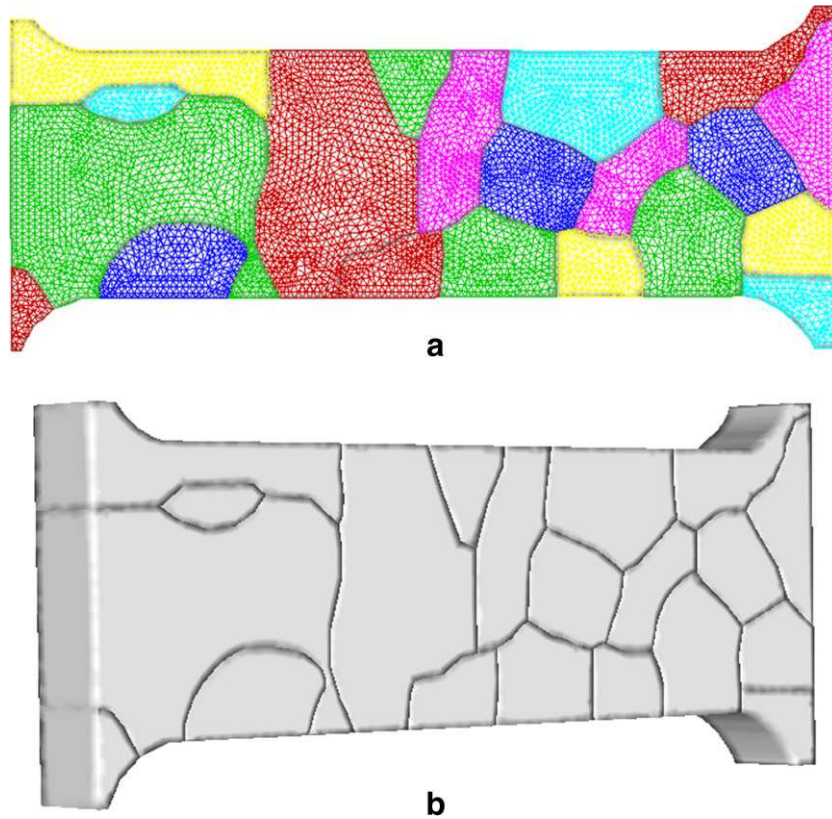


Fig. 2. Computational mesh used in the finite element simulation. (a) The grain boundary profile is identical to that on the top surface of the sample. (b) Each grain has a columnar shape from the extrusion of the grain boundary skeleton lines in the normal through-thickness direction from one surface of the sample to the other.

4.2. Surface strain localization

The evolution of the plastic strain field as obtained by the Digital Image Correlation (DIC) technique on both surfaces of the sample is displayed in Fig. 3. Initially, a strong strain localization effect is observed in grain-6, becoming even more pronounced after 4.76% elongation (Fig. 3d). Eventually, that effect is shown to be dominant in the whole area of grain-6 across the entire width of the sample (Fig. 3f). In contrast to the dominant pattern in grain-6, the plastic heterogeneities in the other grains are more subtle. The strain patterns on both sides of the sample are essentially similar.

Fig. 4 presents a comparison of the in-plane equivalent von Mises strain distribution after 6.18% elongation between the DIC analysis and the simulation result obtained using the crystal plasticity finite element method. The simulation successfully captures the significant strain localization observed in grain-6, where the von Mises strain exceeds 15% at its highest. The simulation captures the strain localization not only inside grain-6 area, but also along the grain boundary between grain-8 and grain-9. This latter localization arises mostly from the interaction between these two grains. In comparison to the dominant

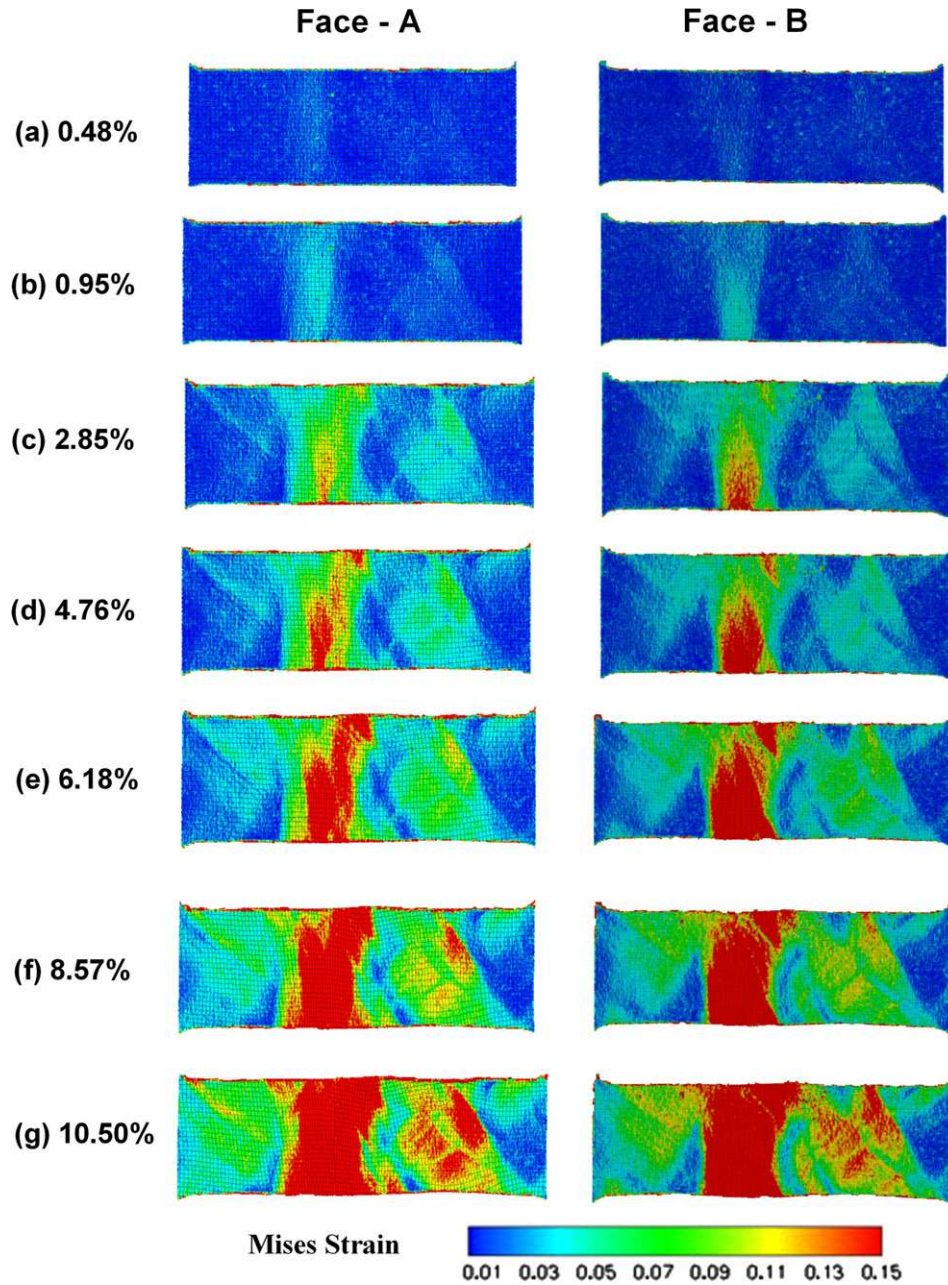


Fig. 3. Evolution of in-plane effective or von Mises strain on both surfaces of the sample during tensile test obtained experimentally using digital image correlation (DIC). The color indicates the von Mises strain obtained from the DIC technique using the in-plane strains. A dominant strain localization can be observed in the area around grain-6. (For interpretation of the references to color in this figure legend, the reader is referred to see the web version of this article.)

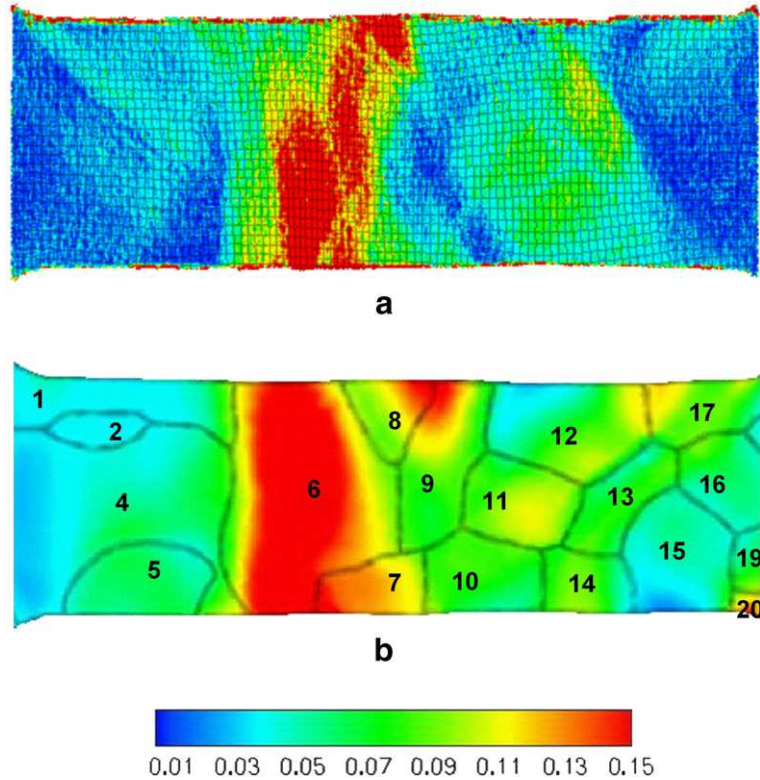


Fig. 4. Comparison of axial surface strain mapping between: (a) experiment and (b) simulation.

strain localization around grain-6, the strain magnitude and heterogeneity are relatively small in the other crystals of the sample. Some discrepancies can also be observed between experiment and simulation. For instance, the strain magnitude inside grain-5 is much lower in the experimental results (Fig. 4a) than that found in the simulation (Fig. 4b). Moreover, the slip bands revealed by the experiments, from grain-1 to grain-4, are not observed by the simulation. The reason for these discrepancies will be discussed in Section 5.

4.3. Surface roughening

The overall roughening profile on surface-A after 10.50% deformation is shown in Fig. 5a. A significant amount of surface roughness can be observed. Half of the surface of grain-6 sinks down and forms a deep valley, as marked by the blue color in Fig. 5a. This is consistent with the strain localization observed inside grain-6, which implies a higher thickness reduction at that location in comparison to the neighboring grains. The roughening profile in the rest of the sample is relatively low. For example, grain-5 shows a clear slope declining from the grain boundary with grain-4 to the edge of the sample. In addition, a clear valley can be observed along the grain boundaries between grains-10, 11, 13 and 14 which is a result of the interaction among those grains.

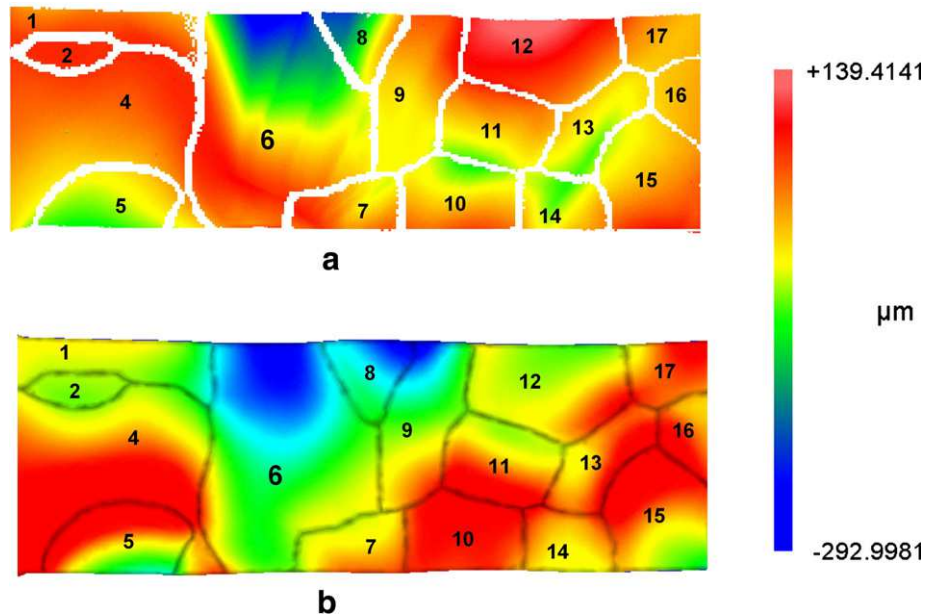


Fig. 5. Comparison of roughening profile on top of the sample between: (a) experimental observation and (b) simulation results from crystal plasticity finite element method.

The corresponding roughening profile obtained from the crystal plasticity finite element simulation is shown in Fig. 5b. A reasonable agreement is found in the grain-6 area where severe strain localization and roughening occur. In addition, the height change in grain-5 is also captured by the simulation. On the other hand, discrepancies between experiment and simulation in the other grains are noticeable. Firstly, the valleys along the grain boundaries between grains-10, 11, 13 and 14 are not properly identified by the simulation. Secondly, the simulated height of grain-1, grain-2 and grain-12 is lower than that provided by the experiment. The reason for these discrepancies is related to the grain geometry distribution through the thickness, which is discussed in Section 5.

4.4. Slip lines on the surface

The slip line pattern on strained crystal's surfaces can assist in the identification of slip system activation. Especially at lower strain levels, this pattern can be used to classify the type of activated slip system. To this end, high resolution measurement of the surface profile conducted in grain-4 reveals the presence of clear slip lines as shown in Fig. 6a and b. The Schmid factors corresponding to uniaxial stress for all 12 f.c.c slip systems inside grain-4 are listed in Fig. 6c, where the angle between all the possible slip lines and the uniaxial tensile axis is also calculated according to the initial grain orientations. The slip system which is marked as No. 7, $(1\bar{1}1) \langle 110 \rangle$, has the maximum Schmid factor of 0.46. Its trace on the surface is a straight line forming an angle of 46° with the tensile loading axis, which closely matches the angle formed by the slip lines observed experimentally.

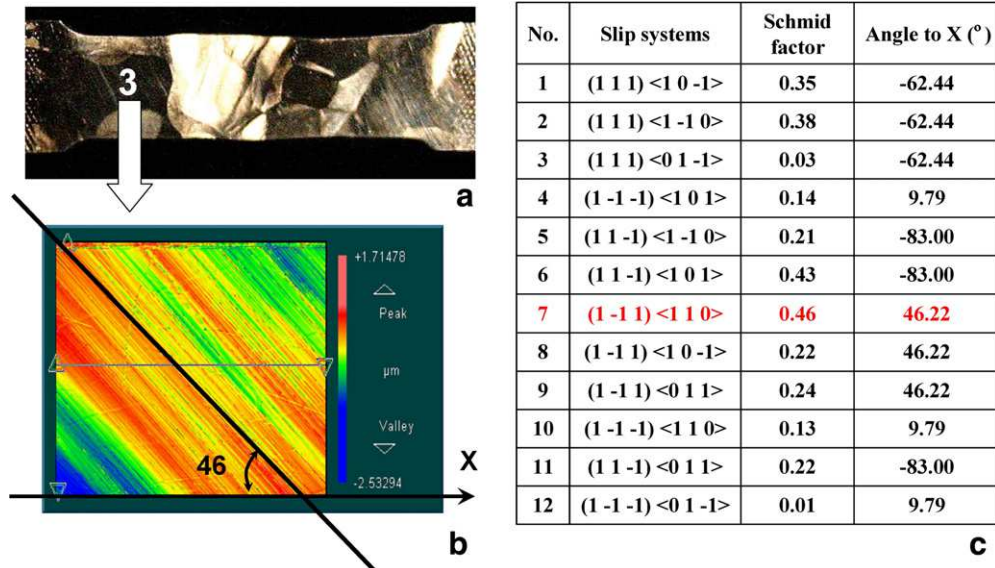


Fig. 6. (a) and (b) Observation of slip lines on the surface of grain-4, (c) Schmid factor analysis. Slip system $(\bar{1}\bar{1}1)$ $\langle 110 \rangle$ has the maximum Schmid factor (0.46). Its trace on the surface has the same inclination as the slip lines observed experimentally.

4.5. Deformed grain shape

The whole area of surface-A is scanned again using EBSD after 10.50% elongation. As shown in Fig. 7a, grain-6, where the deformation localized during the tensile test, experiences internal orientation fragmentation. Additionally, the boundaries among grains-6, 7, 8 and 9 are less visible after straining. Most of the other grains still preserve a relatively uniform orientation distribution with a smooth orientation gradient (see for example grain-13). As illustrated in Fig. 7b, a net of grooves was added to the simulated sample to reveal the deformed grain boundaries. After the simulation and experimental results are overlapped (Fig. 7c), a good match can be found in most of the grains.

4.6. In-grain microstructure and texture

A series of high resolution EBSD measurements with a finer step size ($5 \mu\text{m}$) was conducted inside grain-6 in order to obtain more detailed microstructure information following deformation inside the localization region. As shown in Fig. 8a and b, the deformed grain-6 is characterized by a clear orientation fragmentation with a laminate structure. The originally-uniform orientation is split into several subgrains in the form of a series of orientation bands. A further EBSD line scan, Fig. 8e, proved that there is approximately a 5° orientation change across the banded structure.

Fig. 8c shows the in-grain orientation distribution of grain-6 obtained by high-resolution EBSD in the form of a $\{111\}$ pole figure. The whole grain splits about the transverse direction (TD) into two opposite orientations. This tendency is also clearly captured by the

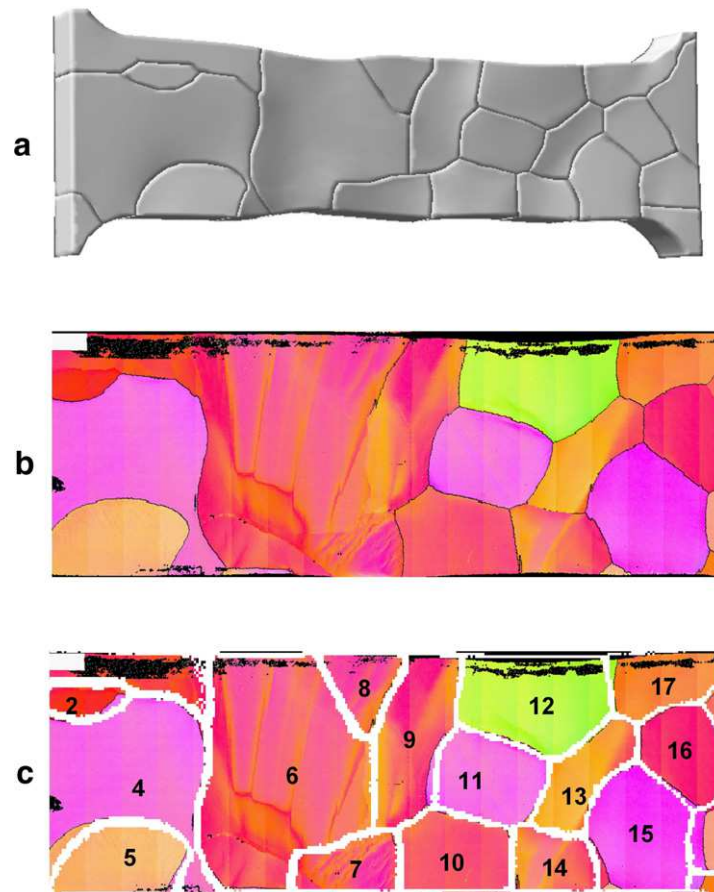


Fig. 7. (a) Comparison of the deformed grain shapes between the simulation and (b) corresponding EBSD observation. (c) A good match can be found after overlapping both results. A perspective view of the simulated specimen is given to emphasize the three-dimensional character of the simulation.

simulation, Fig. 8d, although the magnitude of the scattering is much smaller than in the experimental results.

5. Discussion

The experimental tests of the aluminum oligocrystal samples subject to tensile microscopic deformation exhibit a heterogeneous response characterized by strain localization, surface roughening, grain shape changes, and in-grain texture and microstructure evolution. These phenomena are also observed in the numerical simulations. A quantitative comparison between experiments and simulations examining these phenomena has been provided. The goal has been to elucidate the role of these lower scale deformation features with respect to the heterogeneity of the elastic–plastic deformation of oligocrystals.

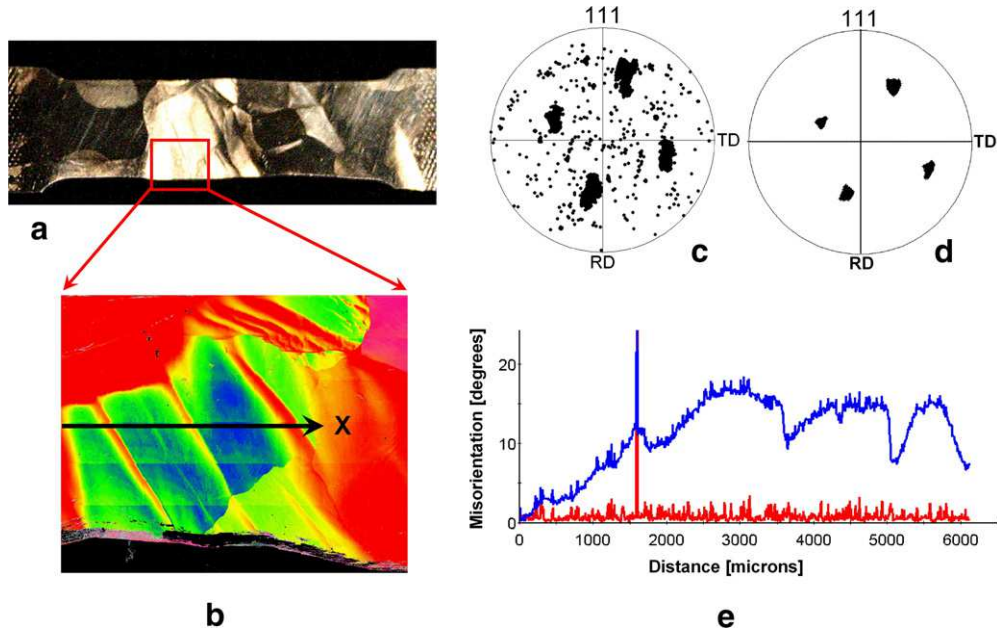


Fig. 8. In-grain fragmentation inside grain-6. (a) Image of deformed dogbone sample. (b) Deformed microstructure revealed by high-resolution EBSD scanning. (c) Deformed orientation distribution in grain-6 revealed using EBSD in $\{111\}$ pole figure. (d) Predicted texture from crystal plasticity finite element simulation. (e) EBSD line scanning along X direction as marked in (b) revealing the orientation changes among the laminate structure.

5.1. Softening in grain-6

A key characteristic observed in this study is the strong softening tendency inside grain-6, as shown in Figs. 4 and 5. A close look at the evolution of the localization during deformation, Fig. 3, suggests that this softening happens from the very beginning of the tensile test, which implies that the orientation of that grain and its initial status are responsible for this behavior.

As discussed by Raabe et al. (2001, 2003), the initial grain orientation contributes to the plastic heterogeneous response in polycrystals, since the resolved shear stress on each slip system depends on its crystallographic orientation under a fixed macroscopic boundary condition. However, this *orientation advantage* seems to be very subtle in the present case. Since all grain orientations occurring in the specimen are rather close to each other, the Schmid and Taylor factor for the imposed loading state are similar as well. This is shown by Fig. 9 which compares the maximum Schmid factors of each grain. The difference between the Schmid factors for all the grains in the gauge section is not very significant, indicating that the grains should all have very similar hardening/softening behavior. As a result, the softening in grain-6 must necessarily arise from another cause. A plausible explanation for the soft response of grain-6 may be found in its lack of constraining effect from its grain neighborhood. As shown in Fig. 2, grain-6 stretches across the whole gauge section without any grain boundary in between. As indicated by the Hall–Petch effect, grain boundaries serve as barriers for dislocation motion. A recent study (Zaefferer

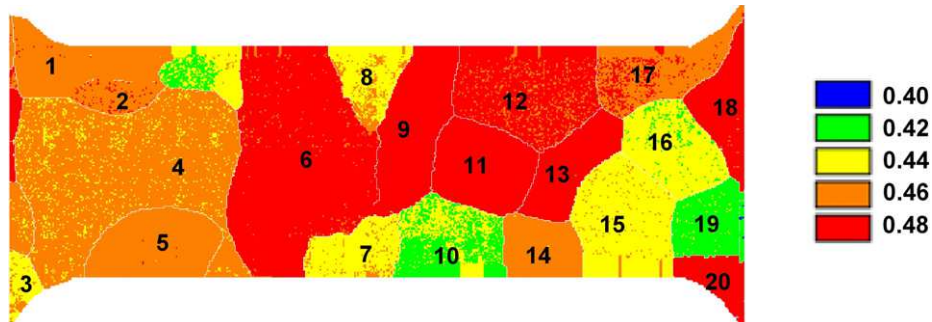


Fig. 9. The distribution of maximum Schmid factor among the 12 f.c.c. slip systems inside each grain.

et al., 2003) has shown that even a small-angle grain boundary can effectively impede the dislocations. Therefore, it is conceivable that in the absence of grain boundaries along the transmission width, dislocations can move freely to the surface perpendicular to the transverse direction, thus providing a mechanism explaining the observed softening response. A related observation is that grains which are embedded within polycrystals experience complex boundary conditions imposed by their neighbors. This is quantified by the difference between the Taylor–Bishop–Hill factor and the Schmid factor in simple homogenization. In other words, grain-6 behaves like a soft single crystal owing to its relatively unconstrained boundary conditions, rather than like a polycrystal grain.

5.2. Roughening

As shown in Fig. 5, the surface roughening observed in this study stems from two different mechanisms: (i) macro-localization (grain-6) and (ii) grain interaction (e.g. grains-10, 11, 13 and 14).

The softening tendency makes grain-6 an area characterized by pronounced strain concentration, with much more significant thickness reduction than in the other grains. As a result, a deep valley is formed, which is well captured by the finite element simulation, as shown in Fig. 5.

On the other hand, the roughening arising from grain interaction has a complex nature, since it is not controlled solely by the mechanical properties of individual texture components but is also influenced by the geometry of the grain boundaries along the thickness direction. This complexity poses additional demands on the model, which are not easy to account for. For example, the simulation does not match the experimental surface profile near grains-10, 11, 13 and 14. This discrepancy is related to the grain profiles and shapes, see Fig. 1, and probably arises from the difference of the grain profiles between the top and bottom surfaces. Fig. 10 shows a schematic of the potential complexities arising from deviations of the grains from a fully columnar structure. These three-dimensional aspects of the geometry give rise to inclined grain boundaries and the appearance of grains on opposite surfaces of the sample which cannot be easily characterized experimentally using non-destructive EBSD measurements on the surface.

Tilted boundaries can serve as a source for a through-thickness shear and ultimately lead to a valley on the surface along grain boundaries. In simulations a simplified columnar grain structure with boundaries perpendicular to the top surface-A is used. As a result,

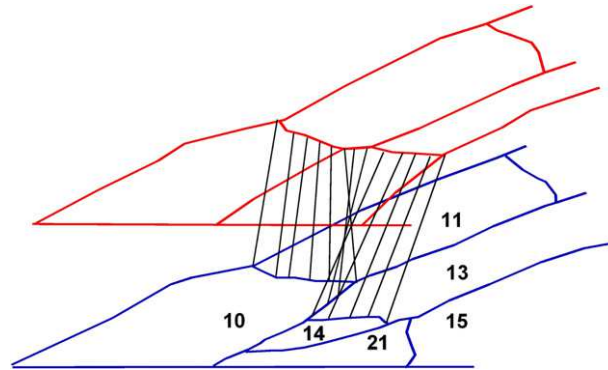


Fig. 10. A schematic plot of a possible grain boundary geometry through the thickness direction. This complexity is likely to introduce additional surface roughening features along some of the grain boundaries.

the thickness reduction of the grains in this area is homogenous because those grains mostly occupy a near-Cube orientation, which has this tendency as pointed out by Zhao et al. (2004).

It should be noted that the roughening profile shows a good agreement between experiment and simulation around grain-4 and 5, Fig. 5, even though a discrepancy exists in the strain mapping, Fig. 4. At least two reasons can be given to explain this discrepancy. Firstly, the subtle band-shape strain localization inside grain-4 seems to originate from the surface slip lines, Fig. 6, since the localization bands and slip lines are approximately parallel, i.e. they both form an angle of about $45\text{--}46^\circ$ with respect to the edge of the sample. Secondly, grain-5 disappears in the middle of the sample through the thickness, as shown in Fig. 1. The part of grain-4 which is beneath grain-5 plays a constraining role impeding the localization of strain in grain-5. In the simulation however, there is a tendency to overpredict the strain level in grain-5 because of the through-thickness interaction with grain-4.

5.3. Local microstructure features

As presented in Fig. 6, the analysis of the slip lines on the top surface of grain-4 proves that the activated slip system experienced a maximum Schmid factor of 0.46, at least at the beginning of plastic straining. It is obvious that the description of slip lines is beyond the capabilities of the model based on a crystal plasticity constitutive approach in which neither the slip systems nor the dislocations are considered explicitly but in an aggregate fashion instead. This excludes the possibility of capturing short range dislocation-based interactions, such as slip line or microband localization effects.

The observation of slip lines on the surface of the deformed sample motivates the investigation of the pattern of slip system activation obtained with the model. To this end, the accumulated slip for all the quadrature points of the elements of grain-4 were averaged for each of the 12 slip systems and compared with the corresponding Schmid factor, Fig. 11. Clearly, the slip system $(1\bar{1}1)\langle 110\rangle$, which has the maximum Schmid factor, has the maximum accumulated slip in the CPFEM simulation. However, other slip systems are also activated, even though their Schmid factors are very low. For instance, the averaged

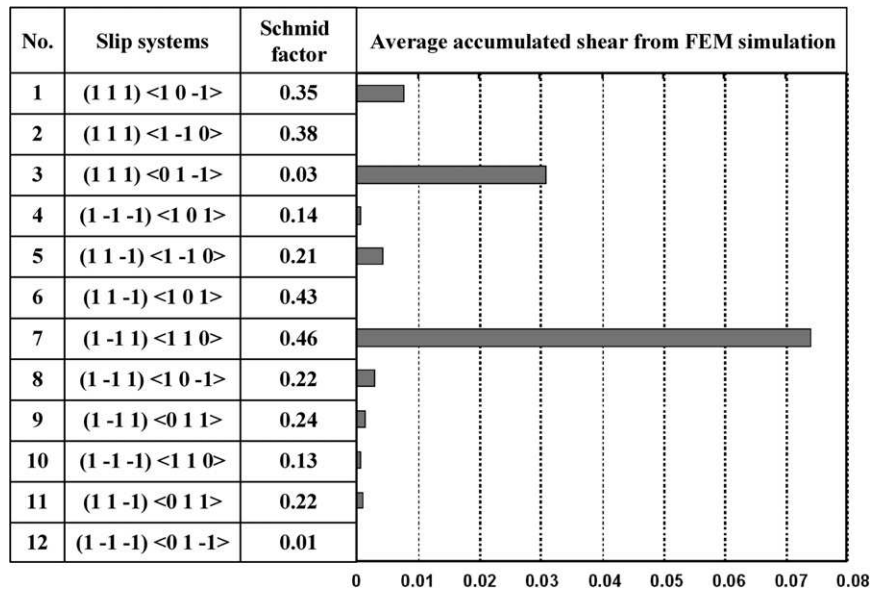


Fig. 11. Correlation between average accumulated slip on each slip system for all the points in grain-4 predicted by the model with the corresponding Schmid factor.

slip of the system (1 1 1) <0 1 $\bar{1}$ > is 0.03 while the Schmid factor for this system is only 0.03. This might arise from the continuum nature of the constitutive model, which theoretically, under Taylor full constraints conditions would lead to the activation of at least five independent slip systems in order to achieve an arbitrary deformation. This may partly explain discrepancies of the model with the actual response.

For grains with larger deformation, the slip line analysis is not a valid procedure for the identification of slip system activation due to grain rotations and in-grain subdivision. This is evident from Fig. 8 which reveals a clear laminate-like microstructure, arising from complex dislocation interactions in the highly-strained grain-6. A number of studies have investigated in-grain orientation fragmentation, using CPFEM (Mika and Dawson, 1998; Raabe et al., 2001, 2002). However, the description of such phenomena in detailed in-grain periodic laminate structures is beyond the capability of the CPFEM approach due to the statistical assumptions inherent in the constitutive laws. Fig. 8c and d also show that the simulated texture in grain-6 is much more stable than that found in the experimental observations. This discrepancy can be explained by the generally meta-stable characteristics of near-Cube f.c.c. texture components. As shown by Raabe et al. (2004), the CPFEM method and related Taylor-type methods have, in some cases, a tendency to overestimate the stability of the Cube orientation or of near-Cube f.c.c. texture components. This occurs where the symmetry of the main active slip systems coincides with the global boundary condition, such as in the case of tensile, compressive, or plane strain compressive states. To avoid this problem, a statistical—albeit realistic—deviation from the ideal Cube orientation can be introduced, which has also been shown to improve the prediction of the overall polycrystal hardening properties (Cheonga and Busso, 2006). In this study, only a uniform orientation was used inside each grain to simplify the numerical studies. This resulted in a lower texture scattering pattern.

6. Conclusions

This study has presented a detailed comparison of crystal plasticity finite element simulation with the experimental uniaxial tensile test on an oligocrystal dogbone specimen. Particular attention has been given to the ability of the model to capture surface roughening, strain localization and the pattern of activation of slip systems in the grains. The following main conclusions are drawn:

- The grain stretching over the whole width of the dogbone specimen is remarkably soft. The absence of dislocation barriers provided by grain boundaries is conducive to strain localization. Due to the significant thickness reduction, a severe surface roughening can be observed in that region of the sample.
- Inclined grain boundaries in otherwise columnar grains can introduce additional shear tendency and a valley-like roughening profile along grain boundaries which leads to discrepancies with the model.
- The appearance of slip lines on the surface at a lower strain level normally arises from the slip systems with maximum Schmid factor. Due to its continuum nature, the crystal plasticity finite element model requires the activation of additional slip systems, besides the one with maximum Schmid factor. An increasing strain can produce a laminate structure which is beyond the capabilities of CPFEM models.

Acknowledgement

The support of DOE through Caltech ASCI Center for the Simulation of the Dynamic Response of Materials is gratefully acknowledged.

References

- Asaro, R.J., Rice, J.R., 1977. Strain localization in ductile single crystals. *Journal of the Mechanics and Physics of Solids* 25, 309.
- Bate, P., 1999. Modelling deformation microstructure with the crystal plasticity finite-element method. *Philosophical Transactions of the Royal Society of London Series A* 357, 1589–1601.
- Beaudoin, A., Bryant, J., Korzekwa, D., 1998. Analysis of ridging in aluminum auto body sheet metal. *Metallurgical Transactions A* 29A, 2323–2332.
- Beaudoin, A., Mecking, H., Kocks, U.F., 1996. Development of localized orientation gradients in fcc polycrystals. *Philosophical Magazine A* 73, 1503–1517.
- Becker, R., 1998. Effects of strain localization on surface roughening during sheet forming. *Acta Materialia* 46, 1385–1401.
- Buchheit, T.E., Bourcier, R.J., Wellman, G.W., Neilsen, M.K., 1997. Capturing the influence of surface constraints in small and thin samples using polycrystalline plasticity theory. *Modelling and Simulation in Materials Science and Engineering* 5, 421–437.
- Cheonga, K., Busso, E.P., 2006. Effects of lattice misorientations on strain heterogeneities in fcc polycrystals. *Journal of the Mechanics and Physics of Solids* 54, 671–689.
- Cuitiño, A.M., 1996. Effect of temperature and stacking fault energy on the hardening of fcc crystals. *Materials Science and Engineering A* 216, 104–116.
- Cuitiño, A.M., Ortiz, M., 1992. Computational modelling of single crystals. *Modelling and Simulation in Materials Science and Engineering* 1, 255–263.
- Delaire, F., Raphanel, J.L., Rey, C., 2000. Plastic heterogeneities of a copper multicrystal deformed in uniaxial tension: experimental study and finite element simulations. *Acta Materialia* 48, 1075–1087.
- Franciosi, P., 1985a. The concepts of latent hardening and strain hardening in metallic single crystals. *Acta Metallurgica* 33, 1601.

- Franciosi, P., 1985b. F.c.c. single crystals hardening: anisotropy and stacking fault energy. In: ICSMA Symposium, Montreal, Canada, p. 281.
- Franciosi, P., 1988. On flow and work hardening expression correlations in metallic single crystal plasticity. *Revue De Physique Appliquee* 23, 383.
- Franciosi, P., Zaoui, A., 1982a. Multislip in f.c.c. crystals: a junction hardening effect. *Acta Metallurgica* 30, 2141.
- Franciosi, P., Zaoui, A., 1982b. Multislip in f.c.c. crystals: a theoretical approach compared with experimental data. *Acta Metallurgica* 30, 1627.
- Franciosi, P., Zaoui, A., 1983. Glide mechanisms in b.c.c. crystals: an investigation of the case of α -iron through multislip and latent hardening tests. *Acta Metallurgica* 31, 1331.
- Havner, K., 1992. *Finite Plastic Deformation of Crystalline Solids*. Cambridge University Press.
- Havner, K., 2005. On lattice and material-frame rotation and crystal hardening on high-symmetry axial loading. *Philosophical Magazine* 85:24, 2861–2894.
- Havner, K.S., 1973. On the mechanics of crystalline solids. *Journal of the Mechanics and Physics of Solids* 21, 383.
- Hill, R., Rice, J.R., 1972. Constitutive analysis of elastic–plastic crystals at arbitrary strains. *Journal of the Mechanics and Physics of Solids* 20, 401.
- Kalidindi, S.R., Bronkhorst, C.A., Anand, L., 1992. Crystallographic texture evolution during bulk deformation processing of fcc metals. *Journal of the Mechanics and Physics of Solids* 40, 537–569.
- Kuchnicki, S.N., Cuitiño, A.M., Radovitzky, R.A., 2006. Efficient and robust constitutive integrators for single-crystal plasticity modeling. *International Journal of Plasticity* 22 (10), 1988–2011.
- Lee, E.H., 1969. Elastic–plastic deformation at finite strains. *Journal of Applied Mechanics* 36, 1.
- Ling, X., Horstemeyer, M.F., Potirniche, G.P., 2005. On the numerical implementation of 3d rate dependent single crystal plasticity formulations. *International Journal for Numerical Methods in Engineering* 63 (4), 548–568.
- Mandel, J., 1972. *Plasticité classique et viscoplasticité*. Tech. Rep., Lecture Notes, Int. Centre for Mech. Sci., Springer, Udine, Berlin.
- McGinty, R.D., 2001. Multiscale representation of polycrystalline plasticity. Ph.D. thesis, Georgia Institute of Technology.
- Mika, D., Dawson, P.R., 1998. Effects of grain interaction on deformation in polycrystals. *Materials Science and Engineering A* A257, 62–76.
- Mika, D., Dawson, P.R., 1999. Polycrystal plasticity modelling of intracrystalline boundary textures. *Acta Materialia* 47 (4), 1355–1369.
- Raabe, D., Sachtleber, M., Weiland, H., Scheele, G., Zhao, Z., 2003. Grain-scale micromechanics of polycrystal surfaces during plastic staining. *Acta Materialia* 51, 1539–1560.
- Raabe, D., Sachtleber, M., Zhao, Z., Roters, F., Zaefferer, S., 2001. Micromechanical and macromechanical effects in grain scale polycrystal plasticity experimentation and simulation. *Acta Materialia* 49, 3433–3441.
- Raabe, D., Zhao, Z., Mao, W., 2002. On the dependence of in-grain subdivision and deformation texture of aluminum on grain interaction. *Acta Materialia* 50, 4379–4394.
- Raabe, D., Zhao, Z., Roters, F., 2004. Study on the orientational stability of cube-orientated fcc crystals under plane strain by use of a texture component crystal plasticity finite element method. *Scripta Materialia* 50, 1085–1090.
- Rice, J.R., 1971. Inelastic constitutive relations for solids: an internal-variable theory and its applications to metal plasticity. *Journal of the Mechanics and Physics of Solids* 19, 433.
- Sarma, G.B., Dawson, P.R., 1996. Effects of interactions among crystals on the inhomogeneous deformations of polycrystals. *Acta Materialia* 44 (5), 1937–1953.
- Shin, H., An, J., Park, S., Lee, D., 2003. The effect of texture on ridging of ferritic stainless steel. *Acta Materialia* 51, 4693–4706.
- Teodosiu, C., 1969. A dynamic theory of dislocations and its applications to the theory of the elastic–plastic continuum. In: Simmons, J.A. (Ed.), *Conference Fundamental Aspects of Dislocation Theory*, vol. 2. National Bureau of Standards Special Publication, Washington, p. 837.
- Teodosiu, C., 1982. *Elastic Models of Crystal Defects*. Springer-Verlag, New York.
- Zaefferer, S., Kuo, J.C., Zhao, Z., Winning, M., Raabe, D., 2003. On the influence of the grain boundary misorientation on the plastic deformation of aluminum bicrystals. *Acta Materialia* 51, 4719–4735.
- Zhang, N., Tong, W., 2004. An experimental study on grain deformation and interactions in an Al–0.5%Mg multicrystal. *International Journal of Plasticity* 20, 523–542.
- Zhao, Z., Radovitzky, R., Cuitino, A., 2004. A study of surface roughening in f.c.c. metals using direct numerical simulation. *Acta Materialia* 52 (20), 5791–5804.